Available online at www.sciencedirect.com

ScienceDirect

journal homepage: http://www.elsevier.com/locate/acme

Original Research Article

# Determination of coupled mechanical and thermal fields using 2D digital image correlation and infrared thermography: Numerical procedures and results

*Marcin Nowak* *, *Michał Maj*

*Institute of Fundamental Technological Research, Polish Academy of Sciences, Pawinskiego 5B, 02-106 Warsaw, Poland*

ARTICLE INFO

*Article history:*
Received 5 May 2017
Accepted 8 October 2017
Available online 17 November 2017

*Keywords:*
Digital image correlation (DIC)
Infrared thermography (IRT)
Coupled thermo-mechanical fields
Aluminum multicrystal

ABSTRACT

The objective of the work is to develop numerical method for determining coupled thermo-mechanical fields based on experimental data obtained from two cameras working in the visible and infrared mode. The sequence of images recorded by the first camera is used to determine the displacement field on the sample surface using the 2D digital image correlation (DIC) method. The resulting field from DIC analysis in a form of a set of discrete points with the corresponding in-plane displacement vector is used as the input for the next step of analysis, where the coupled temperature field is computed. This paper provides a detailed description of the numerical procedures, that allow, to obtain coupled thermal and mechanical fields together with the specification of experimental data needed for calculations. The presented approach was tested on an experimental data obtained during uniaxial tension of the multicrystalline aluminum. The developed numerical routine has been implemented in dedicated software, which can be used for the testing of materials on both a macro and micro scales.



## 1. Introduction

Deformation processes usually proceed in a localized way when considered in both macro and micro scales. Thus, in order to obtain the complete view of the mechanical behavior of the tested material, the field methods of measurement of mechanical quantities should be applied. One of these is the digital image correlation (DIC) method, which for many years has found its application in experimental mechanics as a method for displacement and strain measurements [1,2]. The origin of DIC is the speckle photography technique, which was first published in the early 1980s [3]. From that moment on, the continuous development and improvement of this method has begun. The basic theory and numerical procedures of the DIC were given in [4]. Sutton et al. proposed an improvement of iterative method which reduce computation time in DIC analysis [5]. The next important step in the development of the

* *Corresponding author.*
E-mail addresses: nowakm@ippt.pan.pl (M. Nowak), mimaj@ippt.pan.pl (M. Maj).
https://doi.org/10.1016/j.acme.2017.10.005

**List of symbols**

$\mathbf{x} = (x, y)$ Eulerian coordinate system
$\mathbf{X} = (X, Y)$ Lagrangian coordinate system
$\mathbf{u} = (u_x, u_y)$ in-plane displacement vector
$\mathbf{F}$ deformation gradient
$\mathbf{R}$ rotation matrix
$\mathbf{U}$ stretch tensor
$\mathbf{E}$ Lagrangian strain tensor
$\alpha$ rigid rotation angle
$t$ time
$\mathbf{f}$ reference image gray-level intensity vector
$g$ current image gray-level intensity vector
$c$ correlation coefficient
$\epsilon$ emissivity of the specimen's surface
$T$ temperature

DIC method was application of Newton–Raphson technique as an alternative to the coarse-fine search technique used in calculation of subset deformation [6]. The authors of work [7] gave an extensive review of correlation criteria and algorithms that are mostly used and well established in DIC analysis. Reliability-guided DIC which can be applied for calculation of deformation of objects with complex shapes was given in [8]. Finally the concept (FE)-based global digital image correlation and its comparison to standard subset-based DIC was discussed in [9].

On the other hand, plastic deformation is an irreversible process accompanied by dissipation of energy in form of heat. Therefore, many authors use the infrared thermography (IRT) in order to study thermal effects during deformation process. The main advantage of IRT, is the real time non-contact measurement of temperature distribution on the specimen's surface. In the literature different aspects of thermal effects accompanying the deformation process were analyzed. The paper [10] presents the experimental and theoretical study on stored and dissipated energy evolution and their influence on formulation of isotropic and kinematic hardening law. The propagation of the Lüders band based on thermal data was investigated in [11]. Thermo-mechanical coupling during tension test for austenitic steel was analyzed by the author in [12]. In [13] the IRT was used to study the fatigue in metals taking into account the occurrence of intrinsic dissipation. The analysis of the temperature field was used for determination of the strain localization during static [14] and quasi-static [15] tensile loading. Finally in [16] the experimental method based on IRT and visible imaging was developed for analyzing the energy storage rate distribution in the area of strain localization.

Nevertheless, one of the drawbacks of IRT applied for testing of materials, is the inability to assign the measured temperature of the sample surface to its material point. An infrared camera is directed at the fixed area of space and does not follow the deformation of the sample (Eulerian description of motion). However, in the solid mechanics, a convenient way is to use the Lagrangian description of motion, which allows one to track the change of mechanical fields in time at the material point level. There are many works in the literature in which both techniques are used in order to study thermo-mechanical effects during the deformation process of a wide class of the materials. The localized necking of steel was studied in [17], a notched titanium rolled sheets was experimentally and numerically analyzed in [18] and the coarse-grained aluminum multicrystal was studied during load-unload tensile test in [19].

Usually, the mechanical and thermal fields are determined on opposite sides of the specimen and the obtained results are presented in different coordinate systems [20,16]. This approach allows for the qualitative analysis of obtained results only and is not sufficient in many cases. Nevertheless, there are some papers in which authors determine the coupled mechanical and thermal fields [21,22]. In this case the same area of the specimen is observe simultaneously by two cameras (visible range and InfraRed), using especially designed experimental setup. Then, the displacement field obtained by using separate software is used for tracking the temperature field during deformation. Following the direction of that research, in this paper the algorithm of a traditional DIC 2D method is proposed together with a numerical procedure that extends its ability for coupling the thermal field. The detailed descriptions of the correlation and coupling procedures are presented. The procedures are implemented in the dedicated ThermoCorr software developed by the authors [23]. The software allows for: determination of the displacement field using DIC 2D algorithm, the space and time coupling procedure and carry out the analysis of obtained results. Due to the fact that the obtained data are fully coupled, any further calculation can be made in order to get distributions of other quantities, i.e. plastic work, energy dissipated as heat, etc. This gives the possibility to study the mechanisms of dissipation and energy storage during a deformation process. This paper is organized as follows. In Section 1 a short introduction is presented. Section 2.1 includes the description of experimental data registered simultaneously by two cameras working in visible and infrared mode. This section gives also the basic information about the structure of the input data used for calculation. In Section 2.2 the fundamental concepts of the 2D DIC is presented. Section 3 contains the detailed description of the temperature field determination. The space and time coupling procedure of displacement and temperature fields are shown in Section 4. In Section 5 the methods of determination of strain and rigid rotation are presented. Then, the implementation of presented procedures is shortly described in Section 6. The experimental procedure and results obtained using the developed software for the analysis of uniaxial tension of multicrystalline aluminum are presented in Sections 7 and 8, respectively. Finally, a summary and conclusions are given in Section 9.

## 2. Numerical procedures

### 2.1. *Data acquisition*

The estimation of coupled thermo-mechanical fields requires two independent sequences of data obtained during the

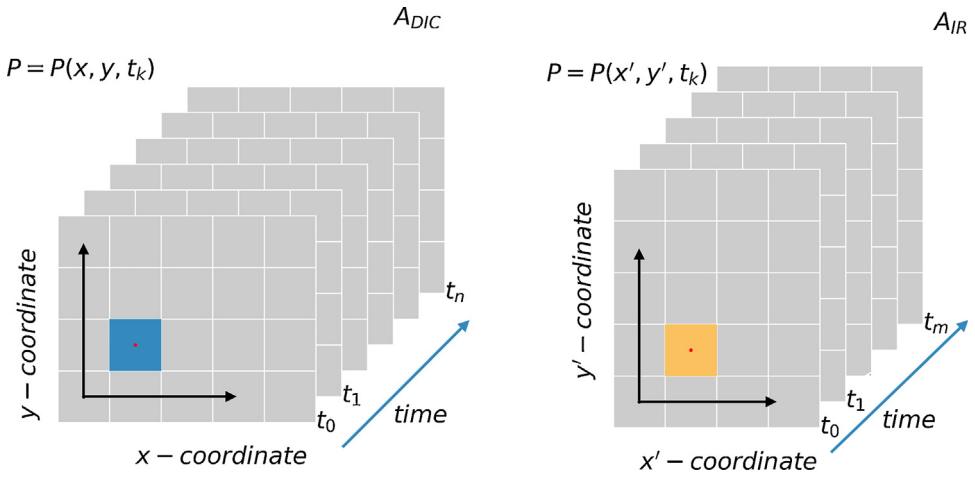


**Fig. 1 – The sequence of images stored as three-dimensional array. (a) Images from the visible range camera $A_{DIC}$, (b) images from the infrared camera $A_{IR}$. Then $n$ and $m$ represent the number of 2D images in time for $A_{DIC}$ and $A_{IR}$ respectively.**

experiment. The first sequence contains the grayscale digital images (usually BMP format) from the visible range camera. Each pixel in the individual image carries information of its intensity value, which can range from 0 for a black color to 255 for a white one. The second sequence contains images recorded by infrared camera. It is worth emphasizing, that neither frequency nor resolution for both measurements has to be the same. Moreover, the shape of the images can also be different as well as for the initial time of registration for both sequences. However, both sets of data must be in the same range of time and space of interest. This is schematically illustrated in Fig. 1.

The sequence of images from the visible range camera denoted by $A_{DIC}$ is used for DIC analysis, whereas the sequence of images recorded by the infrared camera $A_{IR}$ provides the data to thermo-mechanical coupling. Both sequences $A_{DIC}$ and $A_{IR}$ can be treated as three-dimensional array of numbers and they are stored in computer memory as 8-bit integer and 64-bit float numbers respectively. In addition, these arrays possess their own vector of time which arranges the individual images in time order. The HDF5 [24] file format is used to store the arrays on computer disk in a binary file for further use as input data for further calculation.

## 2.2. 2D digital image correlation

The basic concept behind the DIC is to find the new position of a material point in the deformed image, based on its initial position defined on the reference image using its local neighborhood (subset) and the correlation criterion Fig. 2. The issue comes to the calculation of mapping function $\phi$, which deforms subset located in reference configuration (undeformed). The form of the function $\phi$ is determined by applying the correlation criterion of the subset image before and after deformation. The detailed description of correlation criterion is disused in Section 2.2.2.

The subset (neighborhood of material point) may have different shape and size. In practical applications a square or a circle shape is generally used (Fig. 3). Due to the raster type of images, the subset has discrete form. It consists of the points located in the centers of neighboring pixels. The subset size depends on the image resolution and the number of characteristic points on the sample surface (speckled pattern). The size and shape of the subset should provide its uniqueness for the whole image.

For a 2D variation of the DIC method (which is the subject of this work) only one camera working in visible range is needed. The camera axis must be set perpendicular to the plane of the sample and should remain in that position during the whole process. Therefore, it is only possible to measure the in-plane deformation. However, such a measurement is sufficient for many deformation states.

### 2.2.1. Region of interest and mesh

The DIC analysis is preformed only for a finite number of material points located in the center of pixels. Usually, only some part of the sample (its gauge section) is a matter of interest and that region should be defined on the reference image. The center of each pixel inside the region of interest defines the initial coordinates of a material point, and thus the maximum number of material points is equal to the number of pixels in the region. Usually, the calculations are carried out for pixels spaced by a certain step (Fig. 4). The marked pixels are grouped in triangular elements using Delaunay triangulation technique [25]. The result of this operation is a mesh whose nodes are material points. The computed triangles groups the nodes into elements.

The mesh generation allows for the fast detection of neighboring points and for the continuous visualization of a discrete field. The marked material points are indexed and their coordinates are stored in the array $\mathbf{P}$ of size (2, $k_p$) as follows:

$$\mathbf{P} = \begin{pmatrix} X_0 & X_1 & \dots & X_{k_p} \\ Y_0 & Y_1 & \dots & Y_{k_p} \end{pmatrix}, \tag{1}$$

where $k_p$ is the number of material points (nodes) in the region of interest. The element array $\mathbf{T}$ has size (3, $k_e$) and each column of this array contains the three indexes of material

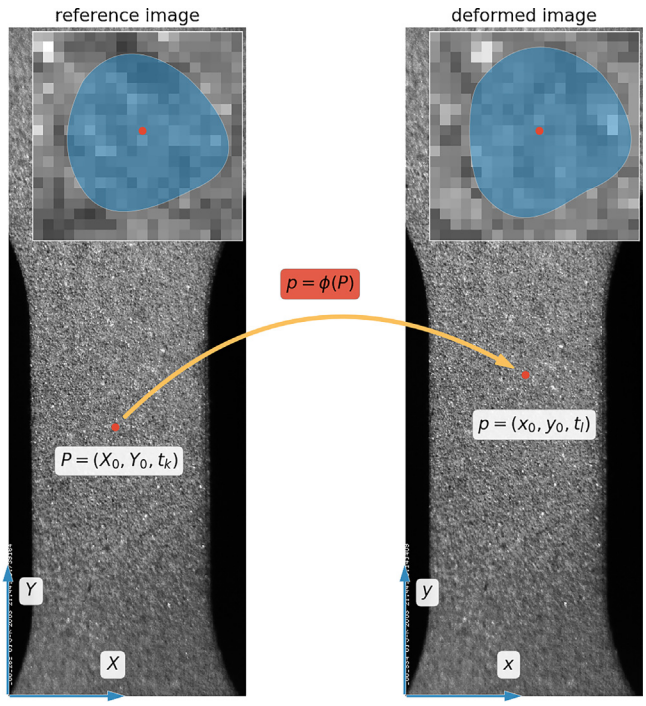


**Fig. 2 – Basic concept of digital image correlation applied for tracking material points during deformation.**

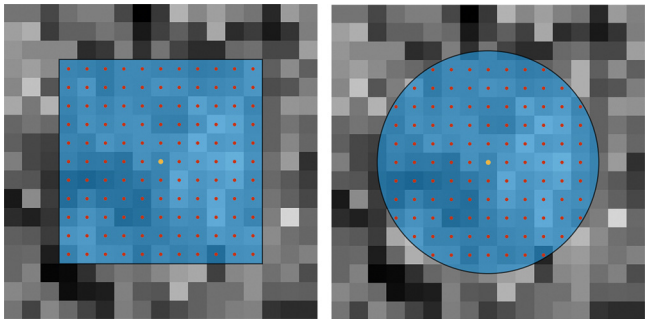

**Fig. 3 – Two types of subset: (a) square, (b) circle. The yellow dots represent the center of the subset whereas the red dots are the neighboring pixels included in subset shape.**

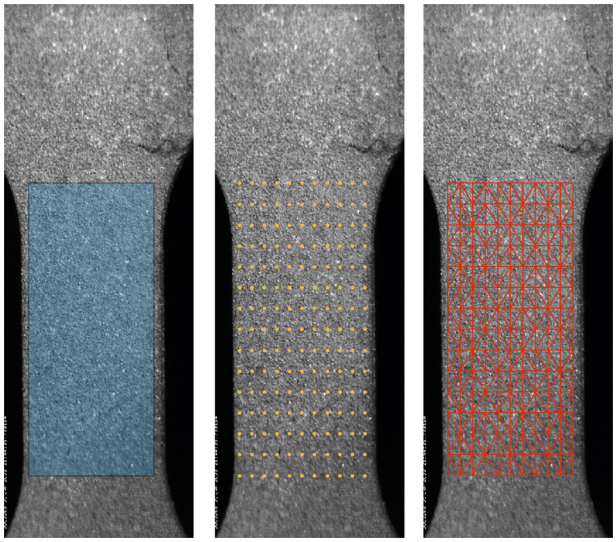

**Fig. 4 – (a) Rectangular region of interest defined on the reference image. (b) The regular set of material points (nodes) located at the center of pixels. (c) Delaunay triangulation for material points (mesh).**

points which form triangular element. Those two arrays are specified for each region of interest and are added to the HDF5 input file.

#### 2.2.2. Correlation criteria

To compare the images of the subset before and after deformation, the correlation coefficient is used. The gray level values of the deformed and undeformed subset are included in the vectors **f** and **g**, respectively. In the literature, the two most commonly used correlation criteria are a Cross-Correlation (CC) and a Sum of Squared Differences (SD). The simplest form of the correlation coefficients based on those criteria are as follows:

$$c_{CC} = \sum_{i=1}^{n} f_i g_i, \qquad c_{SD} = \sum_{i=1}^{n} (f_i - g_i)^2, \tag{2}$$

where the subscript $i$ corresponds to the pixel index and $n$ is the total number of pixels in the subset. In the *CC* criterion, the larger value of correlation coefficient provides a better correlation, whereas in the case of the sum of squared differences, the zero value provides perfect matching. To avoid the influence of illumination changes during the experiment, the correlation criteria are modified by subtracting the mean value of the gray level in the subset. The prefix, 'zero-mean', is added to the name of the criteria and they have the following form:

$$c_{ZCC} = \sum_{i=1}^{n} (f_i - \overline{f})(g_i - \overline{g}), \qquad c_{ZSD} = \sum_{i=1}^{n} [(f_i - \overline{f}) - (g_i - \overline{g}]^2, \tag{3}$$

where $\overline{f} = 1/N \sum_{i=1}^{n} f_i$ and $\overline{g} = 1/N \sum_{i=1}^{n} g_i$. The next step in the way of improving correlation criteria is their normalization. Normalization modifies the equations (2) as follows:

$$c_{NCC} = \frac{\sum_{i=1}^{n} f_i g_i}{\sqrt{\sum_{i=1}^{n} f_i^2 \sum_{i=1}^{n} g_i^2}},$$
$$c_{NSD} = \sum_{i=1}^{n} \left( \frac{f_i}{\sqrt{\sum_{i=1}^{n} f_i^2}} - \frac{g_i}{\sqrt{\sum_{i=1}^{n} g_i^2}} \right)^2. \tag{4}$$

Taking into account the two above modifications, the correlation criteria called the Zero-mean Normalized Cross-Correlation (ZNCC) and the Zero-mean Normalized sum of Squared Differences (ZNSD) have a form:

$$c_{ZNCC} = \frac{\sum_{i=1}^{n} \hat{f}_i \hat{g}_i}{\sqrt{\sum_{i=1}^{n} \hat{f}_i^2 \sum_{i=1}^{n} \hat{g}_i^2}},$$
$$c_{ZNSD} = \sum_{i=1}^{n} \left( \frac{\hat{f}_i}{\sqrt{\sum_{i=1}^{n} \hat{f}_i^2}} - \frac{\hat{g}_i}{\sqrt{\sum_{i=1}^{n} \hat{g}_i^2}} \right)^2, \tag{5}$$

where $\hat{f}_i = f_i - \overline{f}$ and $\hat{g}_i = g_i - \overline{g}$. The correlation coefficient has a limited range of values in order to assess how far form the perfect matching the correlation is. For normalized *CC* criteria the value of $-1$ means perfect mismatching and the value 1 means perfect matching, whereas for normalized *SD* criteria these values are equal to 1 and 0, respectively. In practice, the formula (5), presented above are most commonly in use. However, some additional modifications that take into account the heterogeneity of light conditions may be introduced [8].

#### 2.2.3. Integer-pixel displacement searching scheme

The determination of the position of the material point after deformation can be performed in two steps. In the first step, the displacement vector is determined with an accuracy of one pixel. In the second step the obtained solution is further improved in order to achieve a sub-pixel accuracy. The basic concept of the first step of calculation, called integer-pixel displacement searching scheme is shown in Fig. 5. Initially, on the deformed image the searching area which defines all possible locations of the center of undeformed subset is determined. Then, for each position of the subset the correlation coefficient is calculated, taking the gray level values of overlapping areas.

The calculated correlation coefficients are saved in a two-dimensional array **C**. Each element of this array corresponds to the coordinates of the moving subset center. The maximum of **C** determines the best match and thus the unknown displacement vector Fig. 6.

#### 2.2.4. Peak finding

One of the methods of improving the integer-pixel displacements solution is the application of the peak-finding algorithm in order to detect a fractional part of displacements. The peak-finding algorithm fits the two-dimensional quadratic surface to pixels around the maximum value of correlation coefficient matrix. The positions of the pixel centers are stored in one dimensional vectors as follows:

$$\mathbf{x} = \begin{pmatrix} -1 & -1 & -1 & 0 & 0 & 0 & 1 & 1 & 1 \end{pmatrix}, \tag{6}$$

$$\mathbf{y} = \begin{pmatrix} -1 & 0 & 1 & -1 & 0 & 1 & -1 & 0 & 1 \end{pmatrix}, \tag{7}$$

where the origin of local coordinate system is located at the pixel with maximal correlation coefficient. The distance between center of pixels is equal to 1 and the local matrix has dimensions $3 \times 3$ pixels. To detect the non-integer peak position of the discrete correlation coefficient array, the two-dimensional quadratic surface fitting is applied. The equation of two-dimensional quadratic surface is given by:

$$f(x, y) = ax^2 + by^2 + cxy + dx + ey + f. \tag{8}$$

The unknown coefficients, $a$, $b$, $c$, $d$, $e$, $f$, are stored in vector **p** and are computed using least-squares fitting,

$$\mathbf{X}^T \mathbf{X} \mathbf{p} = \mathbf{X}^T \mathbf{c}, \tag{9}$$

where $\mathbf{X} = \begin{pmatrix} \mathbf{x}^2 & \mathbf{y}^2 & \mathbf{xy} & \mathbf{x} & \mathbf{y} & \mathbf{1} \end{pmatrix}$ and $\mathbf{1} = \begin{pmatrix} 1 & 1 & 1 & 1 & 1 & 1 & 1 & 1 & 1 \end{pmatrix}$. The vector **c** contains the values of correlation coefficient according to the coordinates define in vectors **x** and **y**. The extreme of two dimensional quadric surface is computed by solving the linear system of equations obtained after differentiation of the formula (8),

$$\begin{cases} 2ax + cy + d = 0, \\ 2by + cx + e = 0. \end{cases} \tag{10}$$

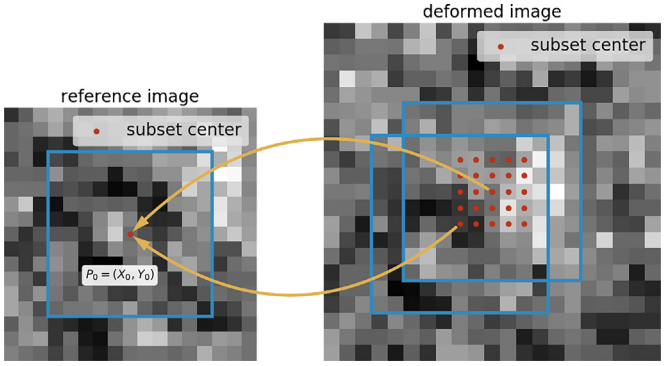


**Fig. 5 – Basic concepts of integer-pixel displacement search. The red dots on the deformed image define searching area (all possible positions of subset center).**

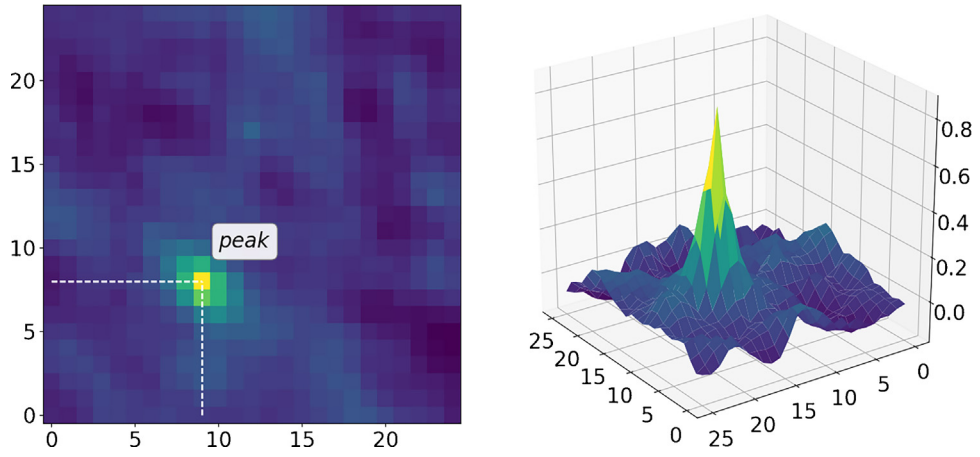


**Fig. 6 – An example of the distribution of correlation coefficient (a) flat view, (b) 2D surface. The peak in the surface corresponds to the maximum value of correlation coefficient (best match between subsets).**

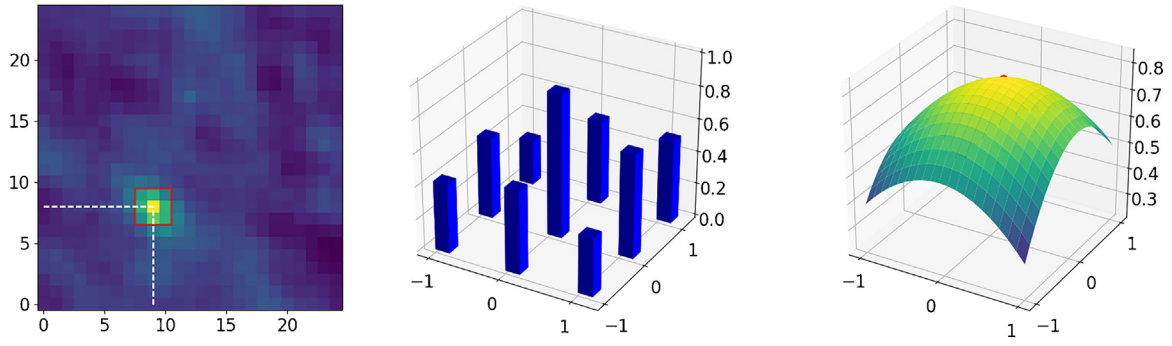

**Fig. 7 – (a) Discrete distribution of the correlation coefficient. (b) Local neighborhood 3 × 3 around the pixel with maximal value of correlation coefficient. (c) The fitted surface to the gray level values of local neighborhood.**

The solution of this system has the following form:

$$x = (dc-ce)/(2ac-2cb), \qquad y = (2ae-2bd)/(2ac-2cb). \tag{11}$$

The computed $x$ and $y$ coordinates define the new sub-pixel position of the peak of correlation coefficient (Fig. 7).

### 2.2.5. *Subset deformation*

The method presented in the previous section does not allow for deformation of the subset and only a rigid translation was taken into account. However, to find the exact location of the subset in the deformed configuration, various forms of its deformation should be considered. One of the many propositions known from the literature, are linear shape functions. Such functions describe the basic deformation scheme illustrated in Fig. 8. To introduce it, let us define the point $\mathbf{P} = (X, Y)$ in the reference configuration. In the deformed configuration this point is expressed as $\mathbf{p} = (x, y)$. The linear shape functions, which map the point from reference configuration into the current one, are as follows:

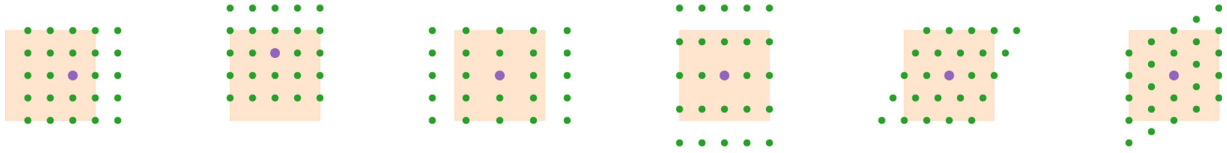

**Fig. 8 – Subset deformation modes: (a) translation in the X direction, (b) translation in the Y direction, (c) stretch in the X-direction, (d) stretch in the Y-direction, (e) shear in the X direction and (f) shear in the Y direction.**

$$x = X + u_x + \frac{\partial u_x}{\partial X}\Delta X + \frac{\partial u_x}{\partial Y}\Delta Y,$$
$$y = Y + u_y + \frac{\partial u_y}{\partial X}\Delta X + \frac{\partial u_y}{\partial Y}\Delta Y, \tag{12}$$

where $\Delta X = X - X_c$ and $\Delta Y = Y - Y_c$. The $X_c$ and $Y_c$ are the coordinates of the subset center. Knowing the values of six parameters, $u_x, u_y, \frac{\partial u_x}{\partial X}, \frac{\partial u_y}{\partial X}, \frac{\partial u_x}{\partial Y}, \frac{\partial u_y}{\partial Y}$, the new subset position is clearly defined.

### 2.2.6. *Newton iteration scheme*

The unknown parameters of the shape functions (Eq. (12)) are stored in a six-component column vector $\mathbf{p}$ as follows:

$$\mathbf{p} = \left(u_x, u_y, \frac{\partial u_x}{\partial X}, \frac{\partial u_y}{\partial X}, \frac{\partial u_x}{\partial Y}, \frac{\partial u_y}{\partial Y}\right)^T, \tag{13}$$

where superscript $^T$ denotes transposition. The vector $\mathbf{p}$, for which the correlation criterion gives the maximum value, can be found using following formula:

$$\frac{dC(\mathbf{p})}{d\mathbf{p}} = \mathbf{0}. \tag{14}$$

Taking a Taylor series around the point $\mathbf{p_o}$ gives:

$$C(\mathbf{p_o} + \boldsymbol{\Delta p}) \approx C(\mathbf{p_o}) + \nabla C(\mathbf{p_o})^T \boldsymbol{\Delta p} + \frac{1}{2}\boldsymbol{\Delta p}^T \nabla\nabla C(\mathbf{p_o})\boldsymbol{\Delta p}, \tag{15}$$

where $\nabla = \sum_{i=1}^{n} \mathbf{e}_i \frac{\partial}{\partial p_i}$. Taking the derivative of Eq. (15) with respect to the vector $\mathbf{p}$ and using Eq. (14) we obtain:

$$\frac{dC(\mathbf{p_o} + \boldsymbol{\Delta p})}{d\boldsymbol{\Delta p}} \approx \nabla C(\mathbf{p_o}) + \nabla\nabla C(\mathbf{p_o})\boldsymbol{\Delta p} = \mathbf{0}. \tag{16}$$

Thus, from Eq. (16) the formula for increment of vector $\mathbf{p}$ has a form:

$$\boldsymbol{\Delta p} = -\frac{\nabla C(\mathbf{p_o})}{\nabla\nabla C(\mathbf{p_o})}. \tag{17}$$

After the calculation of the new increment, the whole procedure is repeated until convergence is obtained. The computation of vector $\mathbf{p}$ requires the calculation of the derivatives of the correlation criterion with respect to vector $\mathbf{p}$. A detailed description of the final formula of those derivatives together with the assumptions needed to neglect some of their parts can be found in [26].

### 2.2.7. *Interpolation*

One of the most important issues in DIC is the interpolation of grayscale intensity of pixels. The subset deformation causes that the points are located at non-integer position. Therefore, the value of grayscale intensity in these positions must be known. The developed program uses bicubic interpolation for calculation of gray-scale values at fractional positions. To calculate them, let us write the fractional part of position vector as:

$$\Delta x = x - \lfloor x \rfloor, \qquad \Delta y = y - \lfloor y \rfloor, \tag{18}$$

where $\lfloor \cdot \rfloor$ denotes the floor function. The value of the gray scale can be obtained from the following formula:

$$g = g(x, y) = \sum_{i=0}^{3}\sum_{j=0}^{3} a_{ij}\Delta x^i \Delta y^j, \tag{19}$$

where $a_{ij}$ is the unknown matrix of coefficients. Differentiating formula (19) with respect to x and y gives

$$\frac{\partial g}{\partial x} = \sum_{i=1}^{3}\sum_{j=0}^{3} a_{ij} i \Delta x^{i-1} \Delta y^j, \qquad \frac{\partial g}{\partial y} = \sum_{i=0}^{3}\sum_{j=1}^{3} a_{ij} j \Delta x^i \Delta y^{j-1}. \tag{20}$$

The cross derivative xy has a form:

$$\frac{\partial^2 g}{\partial x \partial y} = \sum_{i=1}^{3}\sum_{j=1}^{3} a_{ij} ij \Delta x^{i-1} \Delta y^{j-1}. \tag{21}$$

Assuming that the derivatives with respect to x, y and xy and the gray value for all neighboring centers of pixels are known, the coefficients matrix $a_{ij}$ is calculated by substituting their coordinates (Fig. 9) to Eqs. (19)–(21). This leads to the system of linear equations,

$$\mathbf{A}\boldsymbol{\alpha} = \mathbf{F}, \tag{22}$$

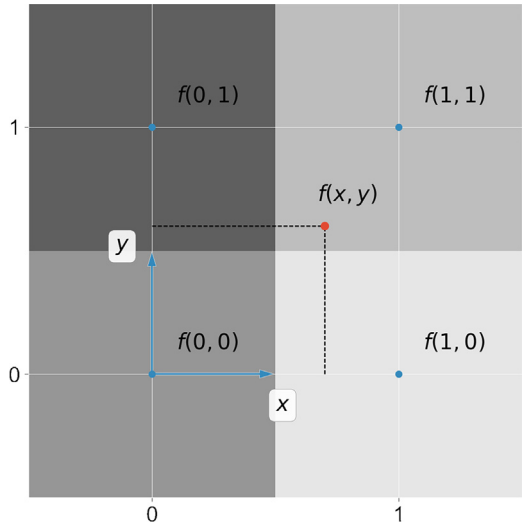


**Fig. 9 – A selected part of a digital image with marked centers of pixels (blue dots) and point at fractional position (red dot) with unknown gray-scale value.**

where $\boldsymbol{\alpha}$ is the flatten matrix $a_{ij}$ in column major order, **A** is the constant matrix of known coefficients and **F** is the column vector containing the gray level value and derivatives at neighboring points. The derivatives $g_x$, $g_y$ and $g_{xy}$ can be computed using central finite differences method.

## 3. Determination of the temperature field

The temperature distribution on the specimen's surface was determined on the basis of the measurement of the infrared radiation from the sample surface using thermographic system assuming that the emissivity value does not change with temperature. The total signal $S_{tot}$ measured by the infrared camera, for non-transparent bodies, can be expressed as follows:

$$S_{tot}(t) = \epsilon S_{obj}(t) + (1-\epsilon)S_{amb}, \tag{23}$$

where $\epsilon$ is the emissivity of the surface and $S_{obj}$ and $S_{amb}$ = -const are the signals corresponding to the signal emitted by the blackbody with temperature equal to the temperature of the object and to the ambient temperature, respectively. Thus, in order to calculate the signal $S_{obj}$ one must know the emissivity of the surface $\epsilon$ and the signal $S_{amb}$. The signal $S_{amb}$ can be determined putting the blackbody working in the differential mode (in this mode the blackbody keeps the temperature of the surroundings) close to the specimen and measure emitted radiation. Therefore, from Eq. (23) the signal $S_{obj}$ is equal to:

$$S_{obj}(t) = \frac{1}{\epsilon}(S_{tot}(t)-(1-\epsilon)S_{amb}). \tag{24}$$

Thus, using the calibration curve $T = \lambda(S)$ (dependence between the signal emitted by the blackbody $S$ vs. its temperature $T$) the temperature of the object $T_{obj}$ can be determined as:

$$T_{obj}(t) = \lambda(S_{obj}(t)). \tag{25}$$

Nevertheless, if the emissivity of the object's surface changes from point to point $\epsilon = \epsilon(X', Y')$ the distribution of the emissivity values must be determined. The $X'$ and $Y'$ are the material coordinates on IRT image. First, the $S_{obj}(X'_0, Y'_0, t_0)$ was determined for the chosen point of known emissivity at the beginning of the process ($t = t_0$) on the basis of Eq. (23). Next, under assumption of uniform temperature of the specimen in the reference state (before the deformation process), the emissivity distribution was determined from Eq. (23) as follows:

$$\epsilon(X', Y') = \frac{S_{tot}(X', Y', t_0)-S_{amb}}{S_{obj}(X'_0, Y'_0, t_0)-S_{amb}}. \tag{26}$$

Thus, substituting Eq. (26) to Eq. (24) and using Eq. (25) one can obtain:

$$T_{obj}(x', y', t) = \lambda\left(\frac{1}{\epsilon(X', Y')}(S_{tot}(x', y', t)-[1-\epsilon(X', Y')]S_{amb})\right). \tag{27}$$

It is worth to notice that the emissivity distribution $\epsilon(X', Y')$ is defined on the reference configuration (Lagrangian coordinates system corresponding to material points), whereas $S_{obj}(x', y', t)$ and $S_{tot}(x', y', t)$ are defined on the actual configuration (Eulerian coordinates system corresponding to the specific location in the space). It means that it is not possible to directly compute the object temperature (Eq. (27)). This issue can be solved as presented in Section 4.

## 4. Coupling of the displacement and temperature fields

So far it was shown how to determine the displacement field for given points on the sample surface by DIC method and temperature field using IRT. The result of DIC analysis is the displacement field for given time steps $\mathbf{u}(\mathbf{X}, t)$. In order to add a new simultaneously measured field (i.e. thermal images registered by IR camera during deformation process) to the results from DIC analysis the coupling procedure must be applied.

First it can be noticed that the experimentally obtained sequences of images from visible and IR cameras are generally in different coordinate systems, have a different resolutions as well as the different frequency of acquisition (Fig. 10). Additionally, the time of acquisition start can be different in both cameras. Therefore following transformation must be determined:

$$\mathbf{p}_{IR} = \psi_s(\mathbf{p}_{DIC}), \qquad t_{IR} = \psi_t(t_{DIC}), \tag{28}$$

where $\mathbf{p}_{DIC} = (x_i, y_i)$ and $\mathbf{p}_{IR} = (x'_i, y'_i)$ are coordinates of the same point in space for DIC and IR images. The $t_{DIC}$ and $t_{IR}$ define the time for DIC and IR image sequences, respectively.

The space transformation $\psi_s$ can be determined by the calculation of the transformation matrix that allow one to find the coordinates of the same point in two frames related to both cameras. Following the concept of [21] the transformation between two coordinates systems related to the visible and the infrared camera is as follows:

$$\mathbf{p}_{IR} = \psi_s(\mathbf{p}_{DIC}) = \begin{pmatrix} a & b \\ c & d \end{pmatrix}\mathbf{p}^T_{DIC} + \begin{pmatrix} e \\ f \end{pmatrix}. \tag{29}$$

The transformation includes translations in the $x$ and $y$ direction, scaling (the same in $x$ and $y$ direction), reflection, and rotation. This gives 5 independent parameters. The transformation parameters can be specified by finding the correspondent coordinates of two different points which lie in the same position on both images and orientation which determines whether a cycle goes round clockwise or counterclockwise from point 1 to point 2. Having those, the coordinates of third point are computed. Substituting the known coordinates of three points into Eq. (29) gives the following system of linear equations:

$$\begin{pmatrix} x'_1 & y'_1 & 0 & 0 & 1 & 0 \\ x'_2 & y_2 & 0 & 0 & 1 & 0 \\ 0 & 0 & x'_1 & y'_1 & 0 & 1 \\ 0 & 0 & x'_2 & y'_2 & 0 & 1 \\ x'_3 & y'_3 & 0 & 0 & 1 & 0 \\ 0 & 0 & x'_3 & y'_3 & 0 & 1 \end{pmatrix}\begin{pmatrix} a \\ b \\ c \\ d \\ e \\ f \end{pmatrix} = \begin{pmatrix} x_1 \\ x_2 \\ y_1 \\ y_2 \\ x_3 \\ y_3 \end{pmatrix}. \tag{30}$$

The solution of above system of linear equations can be easily obtained by applying the Gaussian-elimination method (Fig. 11).

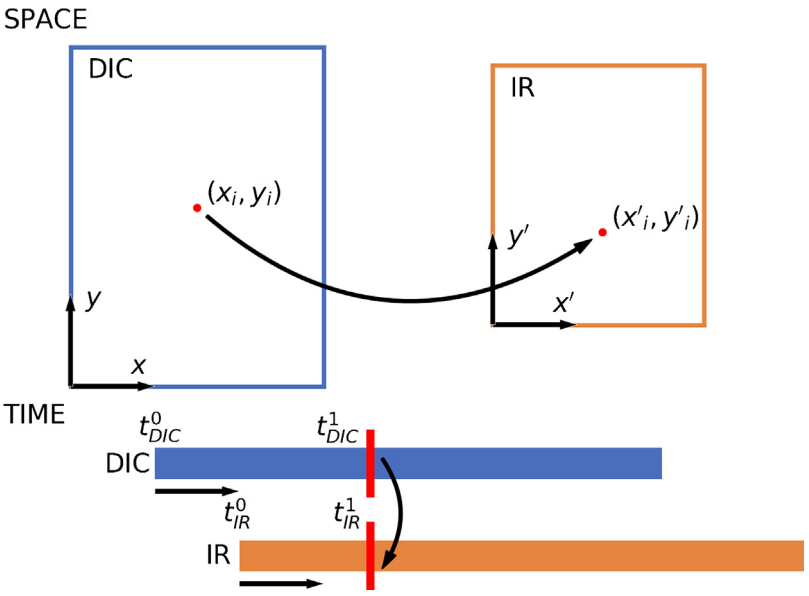


**Fig. 10 – Transformation in space and time between DIC and IR images.**

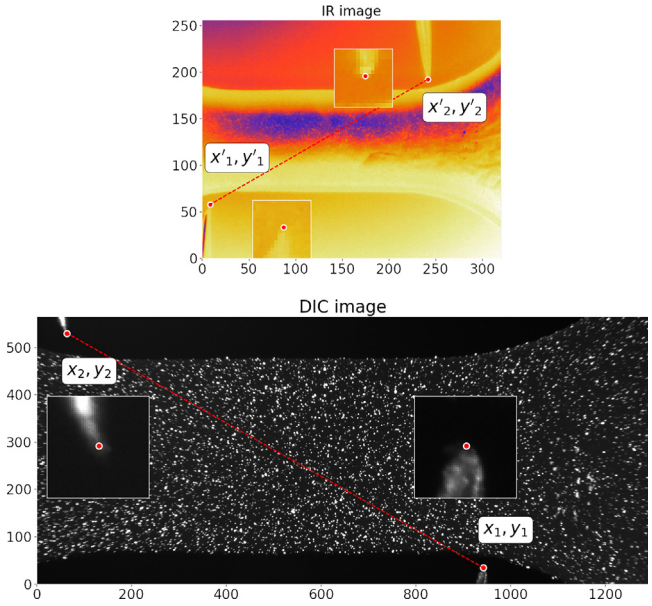


**Fig. 11 – The location of the same points in two different coordinate systems related to images from visible and infrared cameras.**

The next step is to synchronize in time the same process recorded by two cameras. Time shifting is calculated by manually identifying two particular local times associated with the cameras, one for the DIC analysis $t^1_{DIC}$ and the second one for IR images $t^1_{IR}$ (Fig. 10). Both local times should point on the same moment in the process. Then, the time transformation is given by the formula:

$$t_{IR} = \psi_t(t_{DIC}) = t_{DIC} + t^1_{IR} - t^1_{DIC}. \tag{31}$$

Therefore, to obtain coupled thermomechanical field one should:

- find the position on the IR image (X′, Y′) of the material point (X, Y) using space transformation $\psi_s$,
- calculate the emissivity $\epsilon(X', Y')$ from IR image using Eq. (26),
- calculate a new position $(x, y) = (X + u_x, Y + u_y)$ at the time $t_{DIC}$ based on DIC analysis,
- find the corresponding position on the IR image $(x', y')$ of the material point (x, y) using space transformation $\psi_s$,
- find the time $t_{IR}$ using time transformation $\psi_t$,
- find two nearest neighboring IR images to the time $t_{IR}$, read their total signals $S_{tot}(x', y')$ and calculate the interpolated one at the time $t_{IR}$,
- calculate the temperature using Eq. (27).

These steps are repeated for all material points defined in regions of interest and for all instants of time. As a results the coupled mechanical and thermal fields are obtained.

## 5. Computation of strains and rigid rotation

The process of strains calculation comes down to differentiation of the displacement field with respect to the spatial variable. Due to the discrete nature of the displacement field from DIC analysis, the computation of strain needs to be approximated. To calculate the strain tensor at the point (x, y), the local matrix around this point is created. The displacement field at the point of interest is approximated by a plane whose coefficients are calculated with the use of least squares method (Fig. 12). The deformation gradient $\boldsymbol{F}$ for a given position and at a given time can be determined as follows:

$$\boldsymbol{F} = \frac{\partial \mathbf{x}}{\partial \mathbf{X}} = \begin{pmatrix} \frac{\partial x}{\partial X} & \frac{\partial x}{\partial Y} \\ \frac{\partial y}{\partial X} & \frac{\partial y}{\partial Y} \end{pmatrix}. \tag{32}$$

Hence, the deformation gradient $\boldsymbol{F}$ is calculated from the known plane coefficients. The Green-Lagrange strain tensor $\mathbf{E}$ can be obtained as:

$$\mathbf{E} = \frac{1}{2}(\boldsymbol{F}^{\mathrm{T}}\boldsymbol{F} - \mathbf{1}). \tag{33}$$

In order to obtain the rotation angle at particular points on the specimen surface, the polar decomposition of the deformation gradient was used. The right stretch tensor $\boldsymbol{U}$ and rotation tensor $\boldsymbol{R}$ were calculated as follows:

$$\boldsymbol{U} = \sqrt{\boldsymbol{F}^{\mathrm{T}}\boldsymbol{F}}, \qquad \boldsymbol{R} = \boldsymbol{F}\boldsymbol{U}^{-1}. \tag{34}$$

The rotation tensor for the two-dimensional case, under the assumption that the positive angles spin clockwise, has a form:

$$\mathbf{R} = \begin{pmatrix} \cos\alpha & -\sin\alpha \\ \sin\alpha & \cos\alpha \end{pmatrix}. \tag{35}$$

Therefore, the rotation angle can be determined using the following formula:

$$\alpha = \arccos\frac{\mathbf{Re}\cdot\mathbf{e}}{|\mathbf{Re}|\cdot|\mathbf{e}|}\,\mathrm{sgn}(\mathbf{Re}\times\mathbf{e}), \tag{36}$$

where $\mathbf{e}$ is any non-zero vector in 2D plane.

## 6. Program implementation

The developed software uses the procedures presented above composed of two independent parts. The first part is the graphical user interface (GUI) which serves as a pre- and post-processor, whereas, the second part (written in the C language) contains the numerical procedures presented above. The software allows one to determine the displacement, strain, rotation and temperature distributions on the basis of visible range and infrared image sequences. Nevertheless, the first step always has to be performed is the DIC analysis. The DIC analysis consists of three loops Fig. 13a. The first loop refers to the image registered by camera during experiment. In the second loop the individual regions are analyzed. In the third and last parallel loop the consecutive material point are analyzed using the DIC procedure.

In a similar way, the analysis of the strain, rotation and the temperature were implemented. The difference lies in the fact that the first loop is over the calculated frames from DIC analysis Fig. 13b. They can be performed in any order after the analysis of DIC is completed.

## 7. Experimental procedures

The developed software was tested on the basis of experimental data obtained during uniaxial tension of multicrystalline aluminum. The flat sample with the thickness of 0.7 mm and the geometry and dimensions presented in Fig. 14a was electropolished in order to remove the hardened layer after electro-erosion machining. Then, the sample surface was etched in order to reveal the grain boundaries (see Fig. 14b). After that, one surface of the sample was covered by soot (emissivity of about 0.95) and then small drops of white paint (emissivity 0.85) was sprayed onto the same surface (see Fig. 14c). The prepared sample was placed in especially designed mechanical grips limiting the heat exchange between the sample and the testing machine.

The scheme of the experimental setup is presented in Fig. 15a. The main parts of the stand are the testing machine

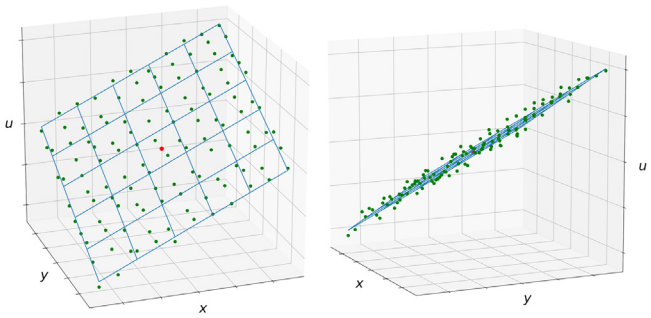


**Fig. 12 – Discrete data of local displacement field around point of interest and its approximation by a plane presented in two different views.**

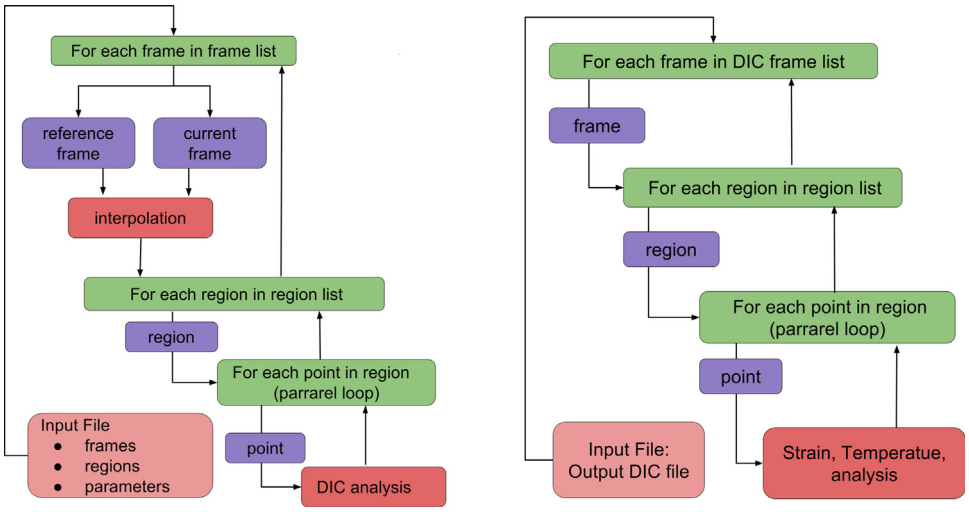


**Fig. 13 – The data flow in the DIC algorithm (a) and in the strain and temperature determination procedures (b).**

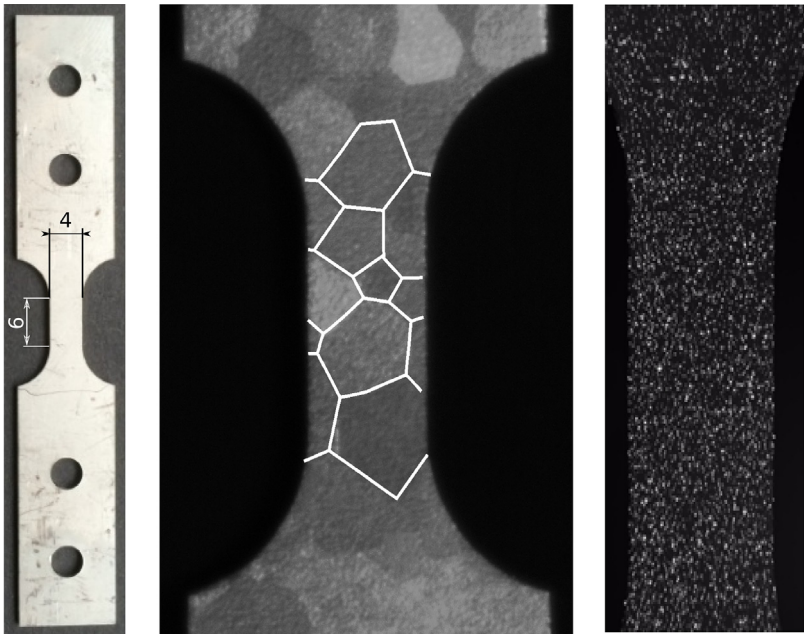


**Fig. 14 – (a) The sample geometry and dimensions, (b) sample surface after etching with mask of grain boundaries and (c) speckle pattern on the specimen surface.**

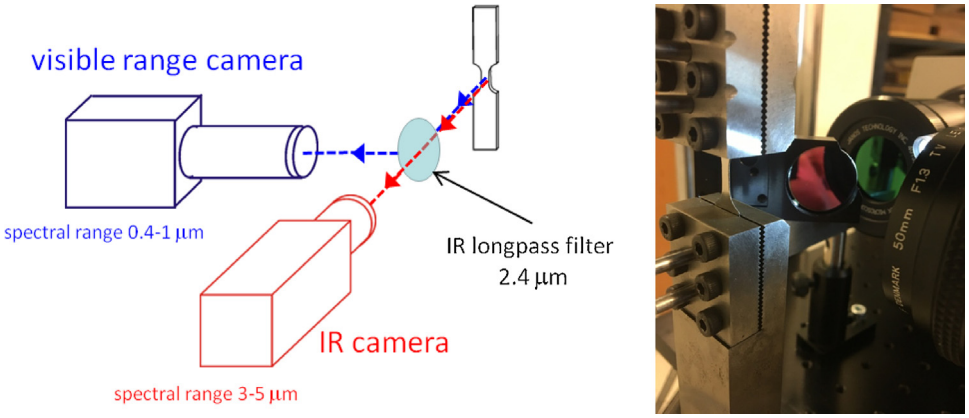


**Fig. 15 – The experimental setup: (a) a scheme, (b) detailed picture.**

**Table 1 – Settings of visible range and infrared cameras.**

| | Manta G-125B | ThermaCam Phoenix |
|---|---|---|
| Resolution [pixel] | 656 × 1292 | 320 × 256 |
| Recording frequency [Hz] | 42.5 | 170 |
| Exposure/integration time [ms] | 1.6 | 3 |
| Pixel size [μm] | 9.5 | 30 |

**Table 2 – Parameters used in DIC analysis.**

| Parameter | Value |
|---|---|
| Subset type | Circle |
| Subset size [pixel] | 20 |
| Newton iterations (max) | 10 |
| Correlation criterion | ZNCC |
| Interpolation type | Bicubic |

and two cameras operating in separate ranges of wavelengths. The basic idea is similar to that presented in [21]. The visible range and the infrared cameras operate at the wavelengths from 0.4 μm to 1 μm and 3 μm to 5 μm, respectively. Thus, using an optical longpass filter, which reflects all incident radiation up to 2.4 μm and transmits over 90 percent of radiation above 2.4 μm and a configuration shown in Fig. 15a, it is possible to set the optical axes of the cameras perpendicular to the same surface of the sample. These are necessary conditions in order to properly measure the temperature distribution using IRT and to apply the 2D DIC algorithm. The distribution of temperature difference was calculated taking into account the distribution of emissivity of the sample surface and knowing the positions of particular material points at every instant of time from the DIC analysis (see Section 3).

The specimen was deformed using a MTS 858 testing machine under displacement controlled uniaxial tension with the strain rate, $\dot{\varepsilon} = 5\times10^{-1}\ s^{-1}$. During straining the force and displacement of the grips were recorded. Simultaneously, the two sequences of images in the visible and infrared ranges were recorded using Manta G-125B and ThermaCam Phoenix cameras, respectively. A comparison of main settings of both cameras used in the experiment is presented in Table 1.

Having both sequences for the same surface of the specimen and using the presented numerical procedures, the evolution of coupled mechanical and thermal fields during deformation of multicrystalline aluminum was determined. The parameters which were used to perform the digital image correlation analysis are shown in Table 2. The correlation scheme with a not updated reference image was used (one image is defined as the reference at the beginning of calculation).

## 8. Results

In Fig. 16a and b the displacement fields $u_x$ and $u_y$ for selected instants of time are presented. The results are shown in the actual configuration (on the deformed specimen). It is seen that the displacement fields are non-uniform from the very beginning of the process. In Fig. 16c the corresponding distributions of correlation coefficient are presented. The high values obtained for the coefficients (not less than 0.98) indicate good accuracy of the obtained displacement fields.

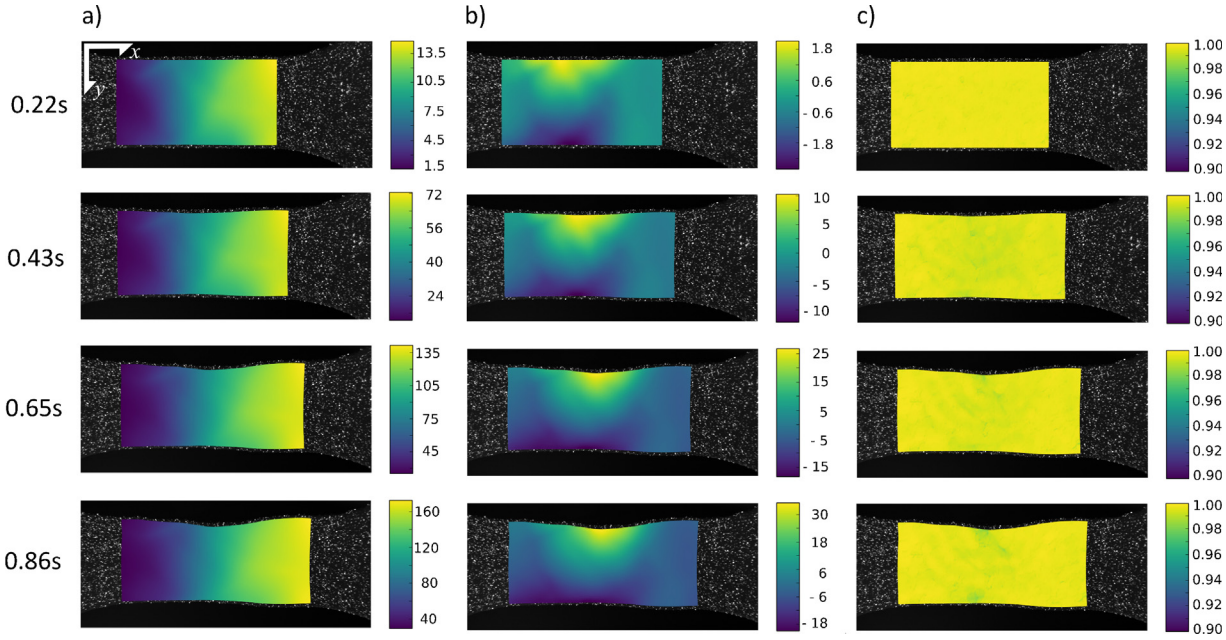


**Fig. 16 – Evolution of the displacement fields (a) $u_x$, (b) $u_y$ and (c) the corresponding distribution of the correlation coefficient.**

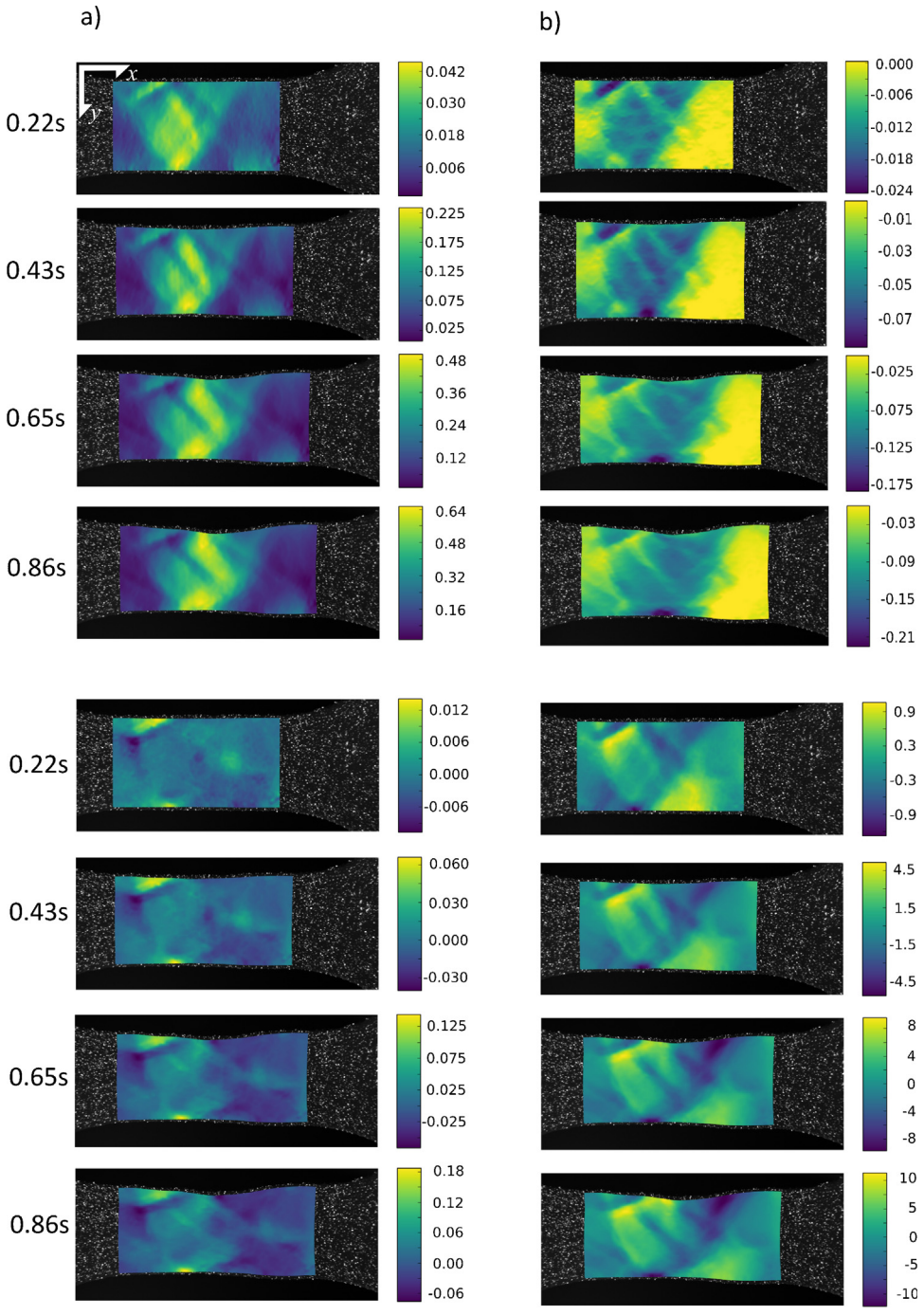


**Fig. 17 – The evolution of strain components (a) $E_{xx}$, (b) $E_{yy}$, (c) $E_{xy}$ and (d) the angle of rigid rotation $\alpha$.**

In Fig. 17 the distribution of Green-Lagrange strain components, $E_{xx}$, $E_{yy}$ and $E_{xy}$ and the rigid rotation angle $\alpha$ calculated on the basis of the obtained displacement field (as demonstrated in Section 5 are presented. Moreover, in Fig. 18 the evolution of the above mentioned quantities and the corresponding temperature difference $\Delta T = T(t) - T_0$ (where $T_0$ is initial temperature) are shown. On the maps presented in the reference configuration, the mask of grain boundaries revealed by etching is placed. It is seen that both mechanical and thermal fields are non-uniform from the very beginning of deformation process. Non-uniform distribution of mechanical and thermal quantities is observed between grains of different orientation but also within particular grains.

## 9. Summary and conclusions

This work presents the detailed description of the developed 2D DIC algorithm and numerical procedures, that allows one to determine the coupled mechanical and thermal fields using DIC method and IRT thermography.

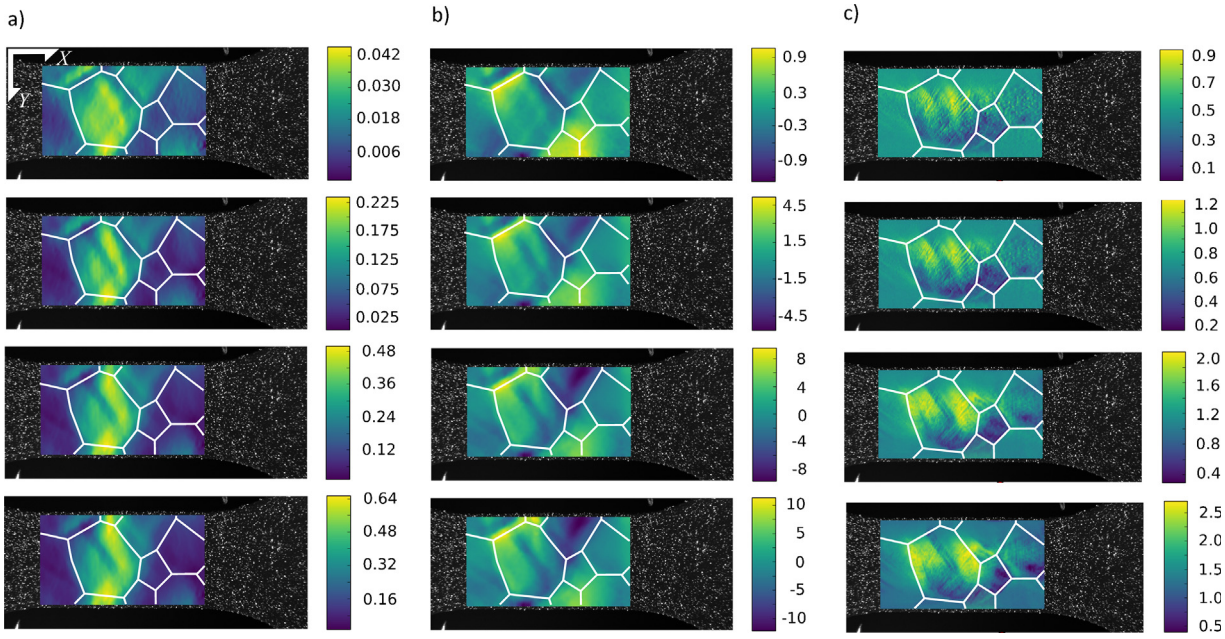


**Fig. 18 – The evolution of strain $E_{xx}$ (a), rotation angle $\alpha$ (b) and the temperature difference distributions $\Delta T$ in the reference configuration (c). Grain boundaries are marked.**

The procedures were implemented in the dedicated software.

The results obtained during deformation of multicrystalline aluminum were presented. It has been shown that proposed approach can be applied to study coupled thermo-mechanical fields taking into account the microstructure of tested material. The determination of fully coupled mechanical and thermal fields (all quantities are determined at exactly the same points) gives one the possibility to perform any operations of the obtained quantities. The presented procedure can be used for any two-dimensional data set. Therefore, it can be easily extended in order to add additional coupled fields, e.g. the distribution of crystallographic orientation obtained using Electron Back-Scattered Diffraction.

## Acknowledgement

The project was funded by the National Science Centre based on the Grant Number 2012/07/D/ST8/02665.

## REFERENCES

[1] T. Gajewski, T. Garbowski, Calibration of concrete parameters based on digital image correlation and inverse analysis, Arch. Civil Mech. Eng. 14 (2014) 170–180.
[2] F. Toussaint, L. Tabourot, P. Vacher, Experimental study with a digital image correlation (DIC) method and numerical simulation of an anisotropic elastic-plastic commercially pure titanium, Arch. Civil Mech. Eng. 8 (3) (2008) 131–143.
[3] W.H. Peters, W.F. Ranson, Digital imaging techniques in experimental stress analysis, Opt. Eng. 21 (3) (1982) 427–431.
[4] T.C. Chu, W.F. Ranson, M.A. Sutton, W.H. Peters, Applications of digital-image-correlation techniques to experimental mechanics, Exp. Mech. 25 (3) (1985) 232–244.
[5] M.A. Sutton, W.J. Wolters, W.H. Peters, W.F. Ranson, S.R. McNeill, Determination of displacements using an improved digital correlation method, Image Vis. Comput. 1 (3) (1983) 133–139.
[6] H.A. Bruck, S.R. McNeill, M.A. Sutton, W.H. Peters, Digital image correlation using Newton–Raphson method of partial differential correction, Exp. Mech. 29 (3) (1989) 261–267.
[7] B. Pan, K. Qian, H. Xie, A. Asundi, Two-dimensional digital image correlation for in-plane displacement and strain measurement: a review, Meas. Sci. Technol. 20 (2009) 17.
[8] B. Pan, Recent progress in digital image correlation, Exp. Mech. 51 (2011) 1223–1235.
[9] B. Wang, B. Pan, Subset-based local vs. finite element-based global digital image correlation: a comparison study, Theor. Appl. Mech. Lett. 6 (2016) 200–208.
[10] A. Chrysochoos, O. Maisonneuve, G. Martin, H. Caumon, J.C. Chezeaux, Plastic and dissipated work and stored energy, Nucl. Eng. Des. 114 (3) (1989) 323–333.
[11] H. Louche, A. Chrysochoos, Thermal and dissipative effects accompanying lüders band propagation, Mater. Sci. Eng. A 307 (1-2) (2001) 15–22.
[12] W. Oliferuk, M. Maj, R. Litwinko, L. Urbanski, Thermomechanical coupling in the elastic regime and elasto-plastic transition during tension of austenitic steel, titanium and aluminium alloy at strain rates from $10^{-4}$ to $10^{-1}$ $s^{-1}$, Eur. J. Mech. A Solids 35 (2012) 111–118.
[13] M.P. Luong, Infrared thermographic scanning of fatigue in metals, Nucl. Eng. Des. 158 (2) (1995) 363–376.
[14] B. Wattrisse, J.-M. Muracciole, A. Chrysochoos, Thermomechanical effects accompanying the localized necking of semi-crystalline polymers, Int. J. Therm. Sci. 41 (5) (2002) 422–427.
[15] M. Maj, W. Oliferuk, Analysis of plastic strain localization on the basis of strain and temperature fields, Arch. Metall. Mater. 57 (4) (2012) 1111–1116.

[16] W. Oliferuk, M. Maj, K. Zembrzycki, Determination of the energy storage rate distribution in the area of strain localization using infrared and visible imaging, Exp. Mech. 55 (2015) 753–760.
[17] A. Chrysochoos, B. Wattrisse, J.-M. Muracciole, Y. El Kaïm, Fields of stored energy associated with localized necking of steel, J. Mech. Mater. Struct. 4 (2009) 245–262.
[18] T. Pottier, F. Toussaint, H. Louche, P. Vacher, Inelastic heat fraction estimation from two successive mechanical and thermal analyses and full-field measurements, Eur. J. Mech. A/Solids 38 (2013) 1–11.
[19] L. Li, J.-M. Muracciole, L. Waltz, L. Sabatier, F. Barou, B. Wattrisse, Local experimental investigations of the thermomechanical behavior of a coarse-grained aluminum multicrystal using combined DIC and IRT methods, Opt. Lasers Eng. 81 (2016) 1–10.
[20] P. Knysh, Y.P. Korkolis, Determination of the fraction of plastic work converted into heat in metals, Mech. Mater. 86 (2015) 71–80.
[21] L. Bodelot, L. Sabatier, E. Charkaluk, P. Dufrenoy, Experimental setup for fully coupled kinematic and thermal measurements at the microstructure scale of an {AISI} 316l steel, Mater. Sci. Eng. A 501 (1-2) (2009) 52–60.
[22] L. Bodelot, L. Sabatier, E. Charkaluk, P. Dufrenoy, Experimental study of heterogeneities in strain and temperature fields at the microstructural level of polycrystalline metals through fully-coupled full-field measurement by digital image correlation and infrared thermography, Mech. Mater. 43 (2011) 654–670.
[23] Thermocorr. http://www.thermocorr.ippt.pan.pl.
[24] Hdf5 library. https://support.hdfgroup.org/hdf5/.
[25] D.T. Lee, B.J. Schachter, Two algorithms for constructing a Delaunay triangulation, Int. J. Comput. Inf. Sci. 3 (1980) 219–242.
[26] G. Vendroux, W.G. Knauss, Submicron deformation field measurements: Part 2. Improved digital image correlation, Exp. Mech. 38 (2) (1998) 86–92.